Journal Name

ARTICLE TYPE

Cite this: DOI: 00.0000/xxxxxxxxxx

Supporting Information to: Unraveling origin of reductive stability of super-concentrated electrolytes from first principles and unsupervised machine learning†

Feng Wang[a] and Jun Cheng*[a]

1 Calculation of redox potentials and computational Li reference electrode

Similar to computational standard hydrogen electrode (cSHE)[1] and computational Ag/AgCl electrode[2] scheme, computational Li reference electrode is proposed as reference for the computed redox potentials in this work. The thermodynamic cycle is given in Fig. S10 a. The Li reference electrode can be expressed in the form of a half redox reaction,

$$\mathrm{Li^+(solv.) + e^-(vac.) \rightarrow Li(s).} \tag{1}$$

Given a redox couple in solution

$$\mathrm{X^\bullet(solv.) + e^-(vac.) \rightarrow X^-(solv.),} \tag{2}$$

the free energy difference of the two half reactions (Eqs. 1 and 2) corresponds to the redox potential with respect to the Li reference electrode.

Equation 1 can be separated into the following two half reactions,

$$\mathrm{Li^+(solv.) \rightarrow Li^+(g),} \tag{3}$$

and

$$\mathrm{Li^+(g) + e^-(vac.) \rightarrow Li(s).} \tag{4}$$

Thus, the redox potential of X/X^- vs. $Li^+/Li(s)$ can be written as the sum of the free energies of the above equations,

$$eU^o = -\Delta_{red}A_X + \Delta_d A_{Li^+} - E_{Li^+} - \mu^{g,o}_{Li^+} - \Delta A_{LJ}, \tag{5}$$

in which $\Delta_{red}A_X$ stands for the reduction free energies of X (equation 2), $\Delta_d A_{Li^+}$ is the desolvation free energy of Li^+(solv.) (equation 3), E_{Li^+} is the total energy of Li^+(g), $\mu^{g,o}_{Li^+}$ is the standard chemical potential of gas phase Li^+ (equation 4) and the ΔA_{LJ} is the free energy correction associated with the formation of cavity in electrolyte.

$\Delta_{red}A_X$ and $\Delta_d A_{Li^+}$ in different electrolytes are computed by ab initio molecular dynamics (AIMD) combined with free energy perturbation (FEP) and thermodynamic integration (TI) method. In the FEP theory, a fictitious mapping Hamiltonian $H_\eta = (1-\eta)H_R + \eta H_P$ is constructed by linear combination of Hamiltonian of reactant H_R and product H_P through the Kirkwood coupling parameter η[3–5]. The free energy difference ΔA can be rigorously obtained by TI, $\Delta A = \int_0^1 \langle \Delta E \rangle_\eta d\eta$, in which the $\langle \Delta E \rangle_\eta$ is the ensemble average of vertical energy gap (i.e. the potential energy difference between reactant and product state at a fixed configuration).

When computing the desolvation free energy of Li^+, a Li^+ is transformed into a dummy atom in the product state, which has no interaction with other atoms in the model. In order to avoid particle overlapping in MD runs, a Lennard-Jones repulsive potential is applied between the dummy atom and other atoms in the simulation model[2]. An artificial cavity is thus created, and the cavity formation free energy ΔA_{LJ} is computed for correction with the finite difference method. Because bond breaking happens spontaneously when adding an excess electron to propylene carbonate (PC) or $TFSI^-$, harmonic bond restraining potentials are applied to maintain the optimal geometries of PC and $TFSI^-$ for computation of reduction integrals.

In addition to the reduction potentials (i.e. redox levels), the vertical energy gaps at endpoints in TI-paths (i.e. $\langle \Delta E \rangle_0$ and $\langle \Delta E \rangle_1$) can be converted into physically meaningful vertical levels, i.e. electronic affinity of oxidized state (EA_X) and ionization potential of reduced state (IP_{X^-}),

$$EA_X = -\langle \Delta_{red}E_X \rangle_0 + \Delta_d A_{Li^+} - E_{Li^+} - \mu^{g,o}_{Li^+} - \Delta A_{LJ}, \tag{6}$$

$$IP_{X^-} = -\langle \Delta_{red}E_X \rangle_1 + \Delta_d A_{Li^+} - E_{Li^+} - \mu^{g,o}_{Li^+} - \Delta A_{LJ}. \tag{7}$$

To demonstrate the accuracy of the computational Li reference electrode, we compute Li^+(aq)/Li(s) potential vs. standard hydrogen electrode (SHE) in aqueous solution. By aligning the absolute potential of Li^+(aq)/Li(s) with respect to computational SHE[4,6], we can obtain

$$e_0 U^{SHE}_{Li^+/Li} = -\Delta_d A_{Li^+} + E_{Li^+} + \Delta A_{LJ} + \Delta_{dp}A_{H_3O^+} - \Delta_{ZP}E + \mu^{g,o}_{Li^+} - \mu^{g,o}_{H^+}, \tag{8}$$

in which $\Delta_{dp}A_{H_3O^+}$ is the deprotonation free energy of H_3O^+ (15.35 eV[7]), $\Delta_{ZP}E$ is zero point correction of H^+(0.35 eV[1]) and the $\mu^{g,o}_{H^+}$ is the standard chemical potential of gas phase H^+ (15.81 eV[6]). Then, to obtain Li^+(aq)/Li(s) potential vs. SHE, we need to calculate the $\Delta_d A_{Li^+}$ and ΔA_{LJ} in bulk water. The computed vertical energies and other details are shown in Fig. S15, and the computed value of $\Delta_d A_{Li^+} - E_{Li^+}$ and ΔA_{LJ} are 9.26 eV and

0.075 eV, respectively. Substituting these numbers into Eq. 8, we can obtain the value of $U^{SHE}_{Li^+/Li}$ of -3.22 V, which is close to the experimental value (-3.04 V).

2 Calculation of dissolution free energies of LiF

The dissolution reaction of solid LiF can be separated into three steps (Fig. S10 b.),

$$\mathrm{LiF(s)} \rightarrow \mathrm{Li(s)} + \frac{1}{2}\mathrm{F_2(g)}, \tag{9}$$

$$\mathrm{Li(s)} \rightarrow \mathrm{Li^+(g)}, \frac{1}{2}\mathrm{F_2(g)} \rightarrow \mathrm{F^-(g)} \tag{10}$$

and

$$\mathrm{Li^+(g)} \rightarrow \mathrm{Li^+(solv.)}, \mathrm{F^-(g)} \rightarrow \mathrm{F^-(solv.)}. \tag{11}$$

Reaction 9 is the reverse of LiF(s) formation from Li(s) and F_2(g) and the corresponding free energy is $-\Delta_f G^o_{LiF}$. Reactions 10 are the formation of gaseous Li^+ and F^- from their standard state Li(s) and F_2(g), and the corresponding free energies are $\mu^{g,o}_{Li^+}$ and $\mu^{g,o}_{F^-}$, respectively. Reactions 11 are the solvation reactions of Li^+ and F^- and the corresponding free energies, $-\Delta_d A_{Li^+}$ and $-\Delta_d A_{F^-}$, can be computed with the FEP-TI method mentioned in the previous section. Thus, the dissolution free energy of LiF can be computed with,

$$\begin{aligned}\Delta_{diss}A_{LiF} = &-\Delta_d A_{Li^+} + E_{Li^+} - \Delta_d A_{F^-} + E_{F^-} + \mu^{g,o}_{Li^+} + \mu^{g,o}_{F^-} \\ &- \Delta_f G^o_{LiF} + 2\Delta A_{LJ},\end{aligned} \tag{12}$$

in which the experimental value of $\mu^{g,o}_{Li^+}$, $\mu^{g,o}_{F^-}$ and $\Delta_f G^o_{LiF}$ are 6.780, -2.757 and -6.054 eV from the handbook[8], respectively. ΔA_{LJ} is the cavity formation energy to correct for the artificial cavity created to keep the dummy atom from other atoms in simulation cells.

3 Computational setup

We investigate PC based electrolytes containing 0, 0.37, 1.11, 1.84, 2.58, 3.69 mol L^{-1} LiTFSI. The cubic supercell with a 16.509 Å linear dimension is used for PC based electrolytes. The ratio of solute and solvent molecules is set according to the experimental density and concentration.[9] The interpolation function between concentration and density is fitted against experiment,

$$\rho(\mathrm{kg\ L^{-1}}) = 0.1073 \times \mathrm{c(mol\ L^{-1})} + 1.2011. \tag{13}$$

AIMD simulations have been carried out using the freely available CP2K/QUICKSTEP package.[10] The molecular orbitals of valence electrons are expanded into DZVP-GTH basis[11], whereas the interaction with the core is described by GTH pseudopotentials[12,13]. The energy cutoff of the plane wave density is set to 500 Ry. The BLYP functional[14,15] is used for all calculations with the Grimme D3[16] dispersion correction.

All initial configurations for Born Openheimer Molecular Dynamics (BOMD) are pre-equilibriated using classical molecular force field MD simulation in the CP2K code. The last configurations from classical MD trajectories are then used for BOMD simulations. The temperature is set to 450 K[17] using Nose-Hoover thermostat to improve sampling and the time step is set to 0.5 fs. After 50 ps BOMD equilibration steps, the final configurations are then used for FEP-TI based free energy calculations.

To improve sampling efficiency, we employ second-generation Car-Parrinello MD (SGCPMD)[18,19] method for free energy calculations. Our simulations run SGCPMD in the canonical ensemble at 450 K for LiTFSI/PC electrolytes, propagating the equations of motion according to the Langevin dynamics and the time step is set to 0.5 fs. γ_L and γ_D is set to 0.001 and 2.2×10^{-4} fs^{-1}, respectively. The timescale for converging vertical energies in free energy calculations is about 5-20 ps for each η. The convergence of vertical energy gaps and thermodynamic integration for free energies are illustrated in Figs. S11, S12 and S13. For the desolvation integrals of Li^+, note that the coordination number between Li^+ and O atoms in PC from our AIMD simulation is about 4 for pure PC (Fig. S8 and S9), which is close to previous AIMD simulation[20] and slightly lower than 4.5 reported in experiment[21,22].

For PC solutions containing $TFSI^-$, localization of inserted electron on $TFSI^-$ would lead to spontaneous decomposition of $TFSI^-$, and thus for computing the one electron reduction potential a harmonic restraining potential is applied to help maintain the integrity of the $TFSI^-$ structure. Restrained bond distances are the equilibrium values from BOMD simulations and the force constant for harmonic restraining potential is 0.1 a.u.[7] In computing solvation free energies of Li^+ and F^-, a Lennard-Jones potential is applied to keep dummy atom from overlapping with other atoms in simulation box when Li^+ or F^- is switched into a dummy. The parameters of the Lennard-Jones potential are σ = 2.337 Å and ε = 0.670 kJ mol^{-1}.[23] Molecular dynamics simulations with classical force fields[24,25] are applied to calculate the cavity formation energies in order to reduce the cost. As demonstrated by Leung et. al.[26], a TI, $\Delta_{LJ}A = \int_0^\sigma \langle \Delta E/\Delta\sigma \rangle_\sigma d\sigma$ with $\Delta\sigma$ = 0.02Å, is used to compute the corresponding cavity formation energy (see Fig. S14). E_{Li^+} is 196.36 eV from BLYP functional and 196.41 eV from HSE06 functional, and E_{F^-} is 658.17 eV from BLYP functional.

Table S1 Details of AIMD models. One PC molecule is replaced by a Li^+ or F^- when computing the desolvation integrals $\Delta_d A_{Li^+}$ and $\Delta_d A_{F^-}$. ρ_{MD} indicates the density of simulation box and ρ (kg L^{-1}) is the density computed by eqn. 13.

c(mol L^{-1})	N_{PC}	N_{TFSI^-}	N_{Li^+}	Box Size (Å)	ρ_{MD} (kg L^{-1})	ρ (kg L^{-1})
0	32	0	0	16.509	1.20	1.20
0.37	30	1	1	16.509	1.24	1.24
1.11	26	3	3	16.509	1.30	1.32
1.84	23	5	5	16.509	1.40	1.40
2.58	19	7	7	16.509	1.46	1.48
3.69	14	10	10	16.509	1.59	1.60

Table S2 Computed energies (eV) for PC solutions containing 0, 0.37, 1.11, 1.84, 2.58 and 3.69 mol L^{-1} LiTFSI. $\Delta_{red}A$ is the reduction integral for inserting an extra electron into electrolyte. $\Delta_d A_{Li^+}$ is the desolvation integral for removing a Li^+ ion from solution phase. $\Delta_d A_{F^-}$ is the desolvation integral for removing a F^- ion from solution phase. ΔA_{LJ} is the energy correction for the Lennard-Jones potential applied to keep the dummy atom away from other atoms. e_0U^o is the computed reduction potential *vs.* $Li^+/Li(s)$. $\Delta_{diss}A_{LiF}$ is the dissolution free energy of LiF. Conduction band minimum (CBM) and valence band maximum (VBM) *vs.* $Li^+/Li(s)$ are computed from averaged vertical energies using equilibrated trajectories at η endpoints. The results are computed using BLYP functional, and the values in parentheses are computed using HSE06 functional from the BLYP trajectories. For c = 0 mol L^{-1}, the computed redox potential is for PC/cPC$^-$ (U^o_{PC/cPC^-}). In order to obtain redox potential of PC/oPC$^-$ (U^o_{PC/oPC^-}), free energy difference of ring-opening of cPC$^-$ is added to U^o_{PC/cPC^-}. U^o_{PC/oPC^-} = 1.25 V *vs.* $Li^+/Li(s)$ by BLYP functional and 0.91 V *vs.* $Li^+/Li(s)$ by by HSE06 functional.

$c(molL^{-1})$	$\Delta_d A_{Li^+}$	$\Delta_d A_{F^-}$	$\Delta_{red}A$	ΔA_{LJ}	e_0U^o	$\Delta_{diss}A_{LiF}$	CBM	VBM
0	206.50 (206.43)	658.08	3.25 (3.41)	0.06	0.05 (-0.23)	0.14	-0.30 (-0.82)	4.97 (6.14)
0.37	206.44 (206.43)	657.80	2.28 (2.19)	0.06	0.96 (1.04)	0.48	-0.13 (-0.39)	4.84 (6.07)
1.84	206.83 (206.74)	657.52	2.16 (2.10)	0.07	1.46 (1.38)	0.39	0.50 (0.11)	5.01 (6.09)
3.69	207.11 (207.07)	656.67	2.05 (1.91)	0.11	1.81 (1.86)	1.05	0.97 (0.72)	4.95 (6.08)

Table S3 The averaged coordination number of Li^+ and O atoms in PC and $TFSI^-$, and F^- and H atoms in PC from the trajectories in calculation of dissolution free energies. Cutoff radii are set to the first minima of of the corresponding radial distribution functions.

$c(\text{mol L}^{-1})$	Li^+-O	F^--H
0	4.02	7.97
0.37	3.96	7.12
1.84	3.98	7.16
3.69	4.02	6.48

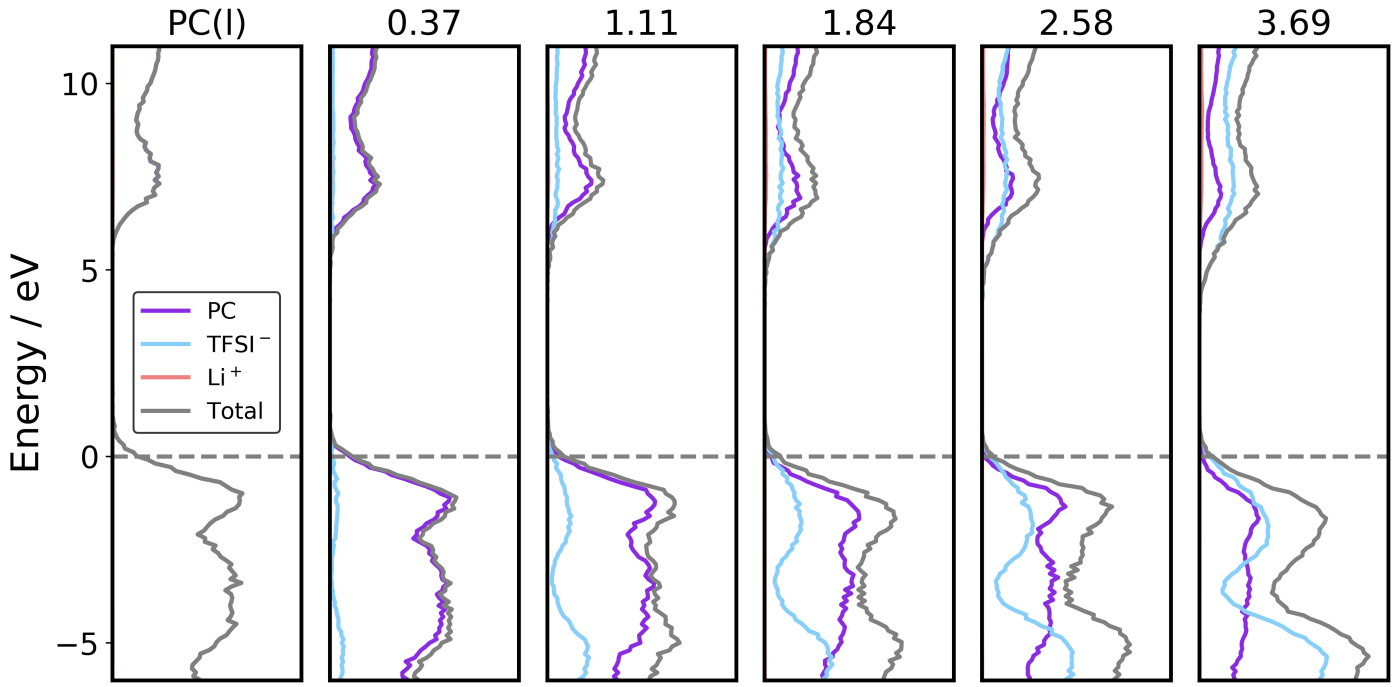

Fig. S1 Electronic projected density of states (PDOS) of PC with 0, 0.37, 1.11, 1.84, 2.58 and 3.69 mol L^{-1} LiTFSI computed using HSE06 functional every 50 fs along the AIMD trajectories of BLYP functional.

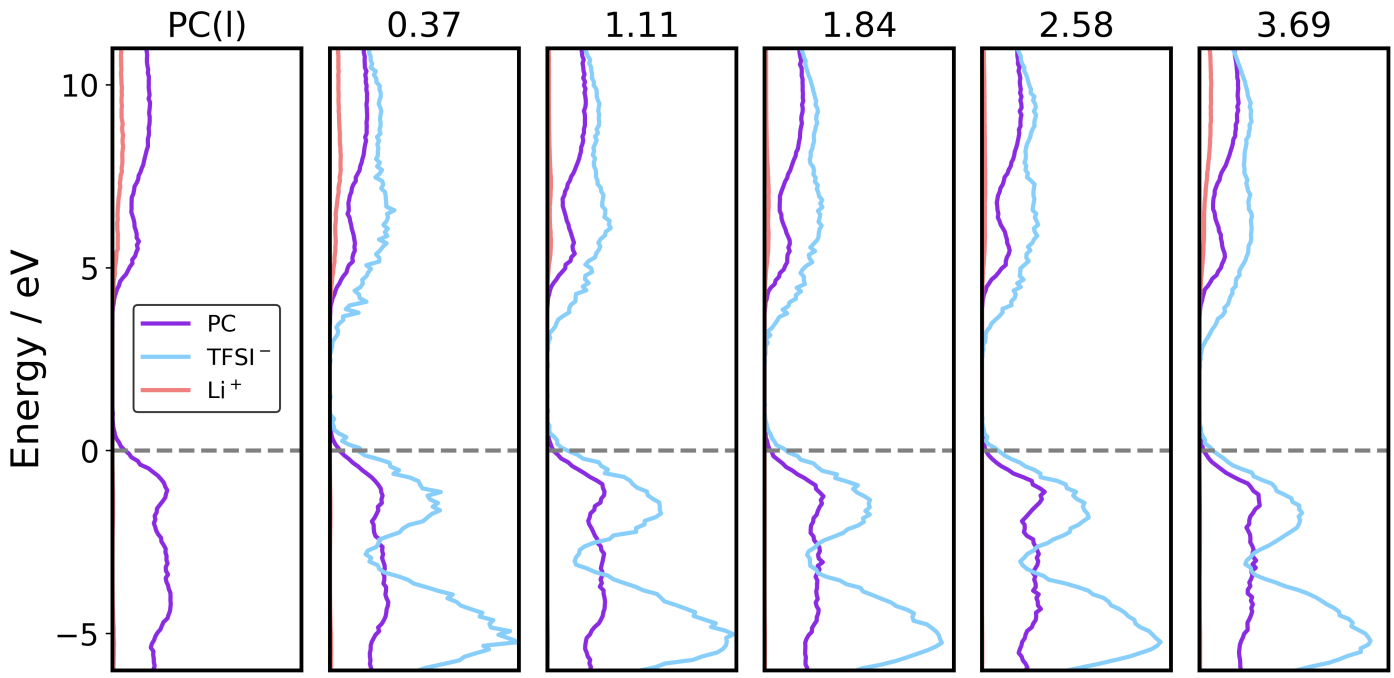

Fig. S2 Normalized electronic projected density of states (PDOS) of PC with 0, 0.37, 1.11, 1.84, 2.58 and 3.69 mol L^{-1} LiTFSI. They are averaged over AIMD trajectories and normalized with respect to the numbers of molecules or ions in simulation cells.

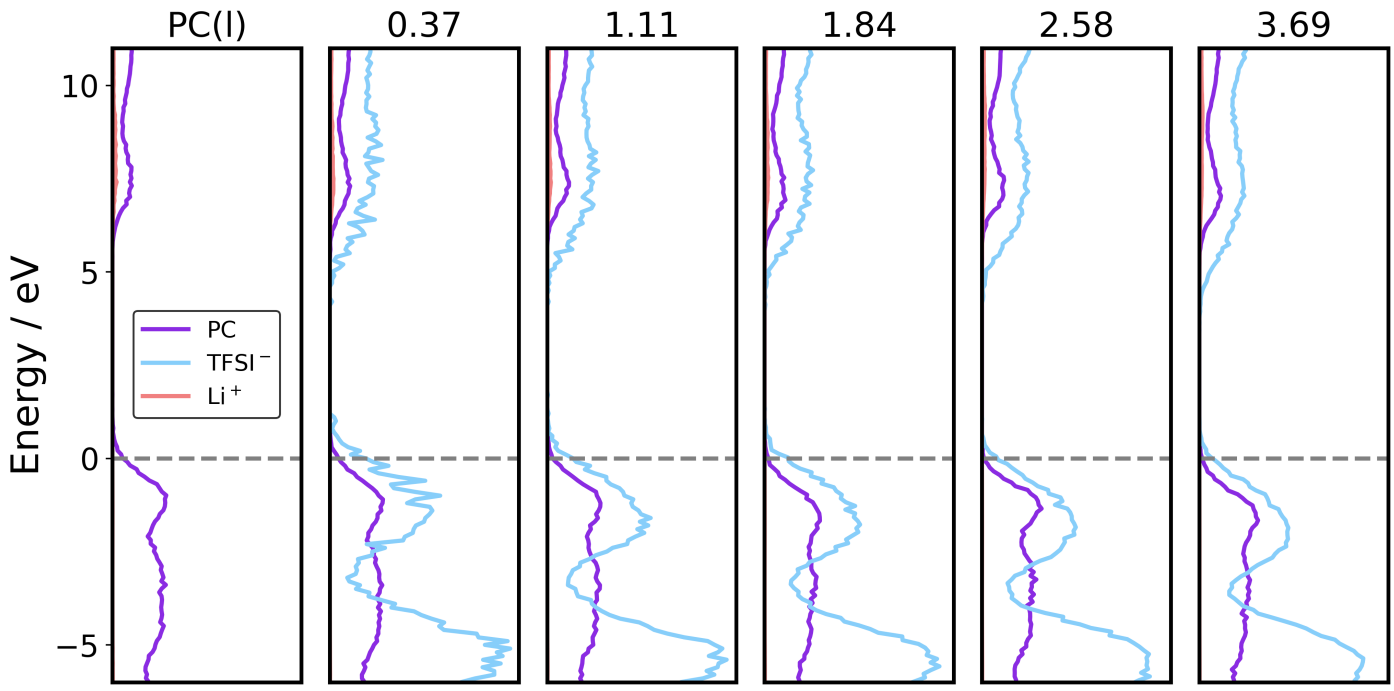

Fig. S3 Normalized electronic projected density of states (PDOS) of PC with 0, 0.37, 1.11, 1.84, 2.58 and 3.69 mol L^{-1} LiTFSI computed using HSE06 functional every 50 fs along the AIMD trajectories of BLYP functional. They are averaged over AIMD trajectories and normalized with respect to the numbers of molecules or ions in simulation cells.

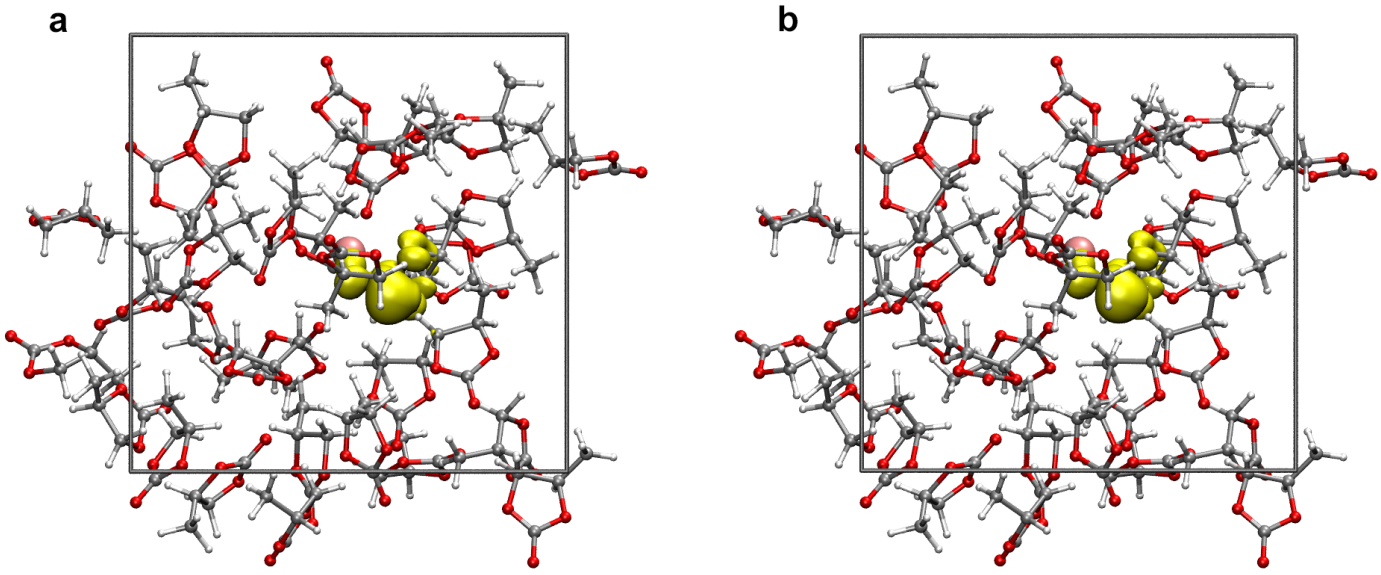

Fig. S4 Spin density distributions of the last snapshots of AIMD trajectories of simulation box consisting of a Li^+ and 31 PC with one extra electron computed by using (a) BLYP and (b) HSE06 functional. Both BLYP and HSE06 can localize the electron on a PC molecule. Color code: O, red; C, gray; H, white; Li, pink; spin isosurface, yellow surface.

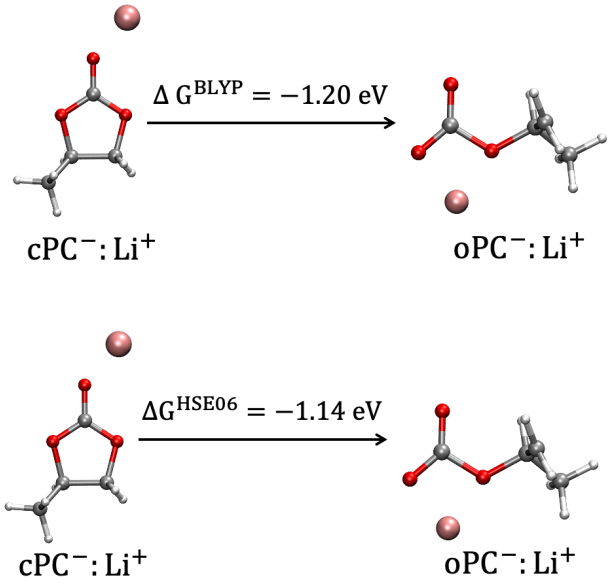

Fig. S5 Gibbs free energy difference between ring-opened PC anion (oPC$^-$) and cyclic PC anion (cPC$^-$) coordinated with one Li$^+$. Color code: Li, pink; O, red; C, gray; H, white. The structures are obtained by static optimization with implicit solvation model SMD of $\varepsilon = 40$[27], by using Gaussian 16 package[28]. The BLYP and HSE06 functional and 6-31+G** basis set are used.

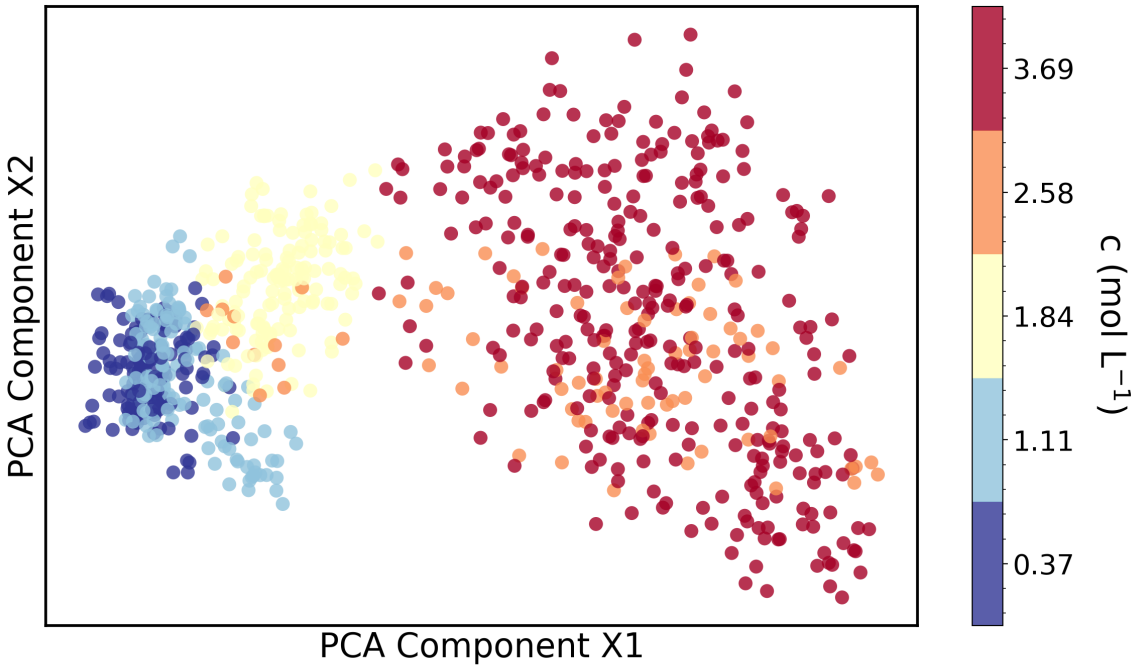

Fig. S6 Unsupervised machine learning of solvation environments of $TFSI^-$ in PC solution at a range of concentrations. $TFSI^-$ anions are randomly selected from AIMD trajectories of PC electrolytes with 0.37, 1.11, 1.84, 2.58 and 3.69 mol L^{-1} LiTFSI. Color coding indicates the concentrations of electrolytes.

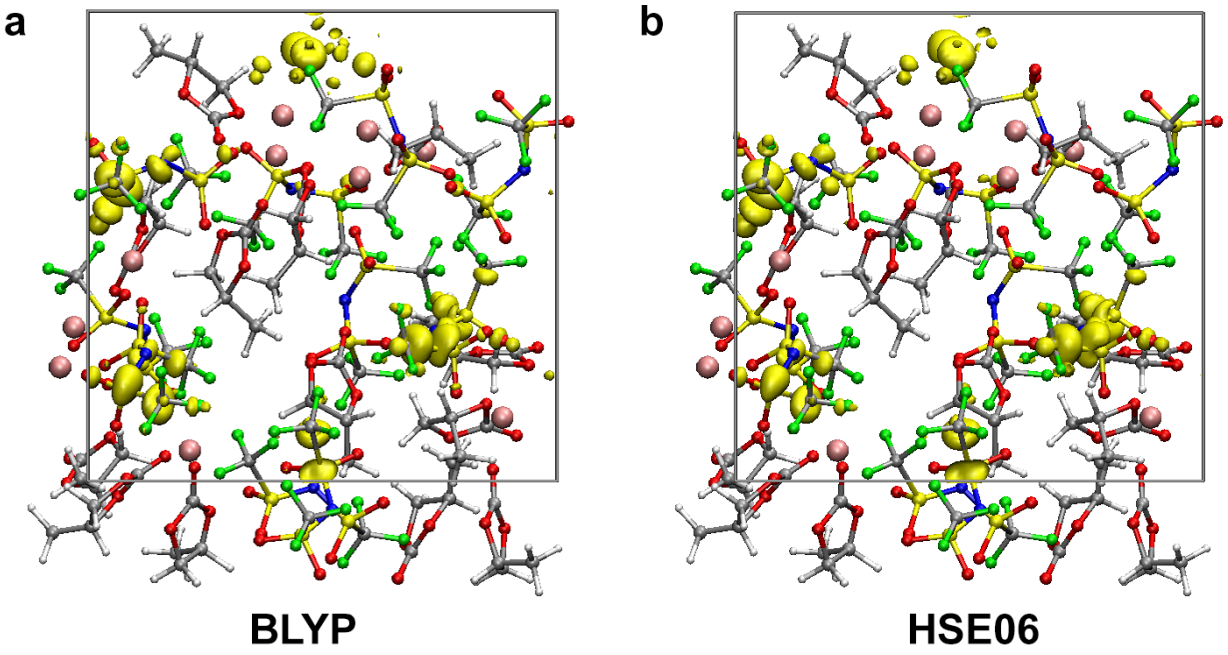

Fig. S7 Density distributions of vertical inserted electrons of the last snapshots of AIMD trajectories of 3.69 mol L^{-1} electrolyte computed by using (a) BLYP and (b) HSE06 functional. Color code: O, red; C, gray; H, white; Li, pink; spin isosurface, yellow surface.

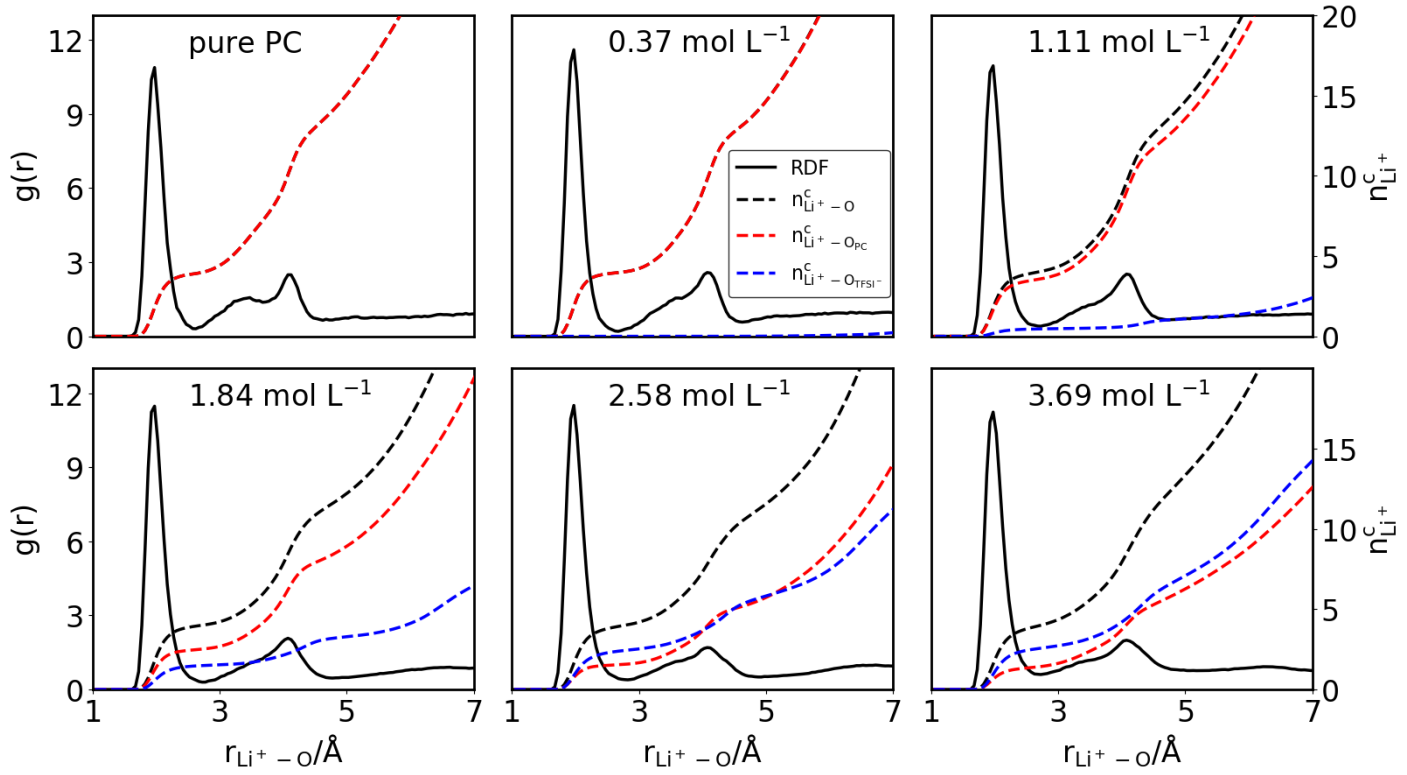

Fig. S8 Radial distribution functions (RDF) for Li^+ to O atoms in PC electrolyte solutions at different LiTFSI concentrations. The RDF are plotted with black solid lines with the left side of the y-axis (g(r)), while integration curves (coordination number, $n^c_{Li^+}$) are dash lines. Black dash lines correspond to all O atoms surrounding Li^+, and red and blue dash lines are for O atoms in PC and $TFSI^-$, respectively.

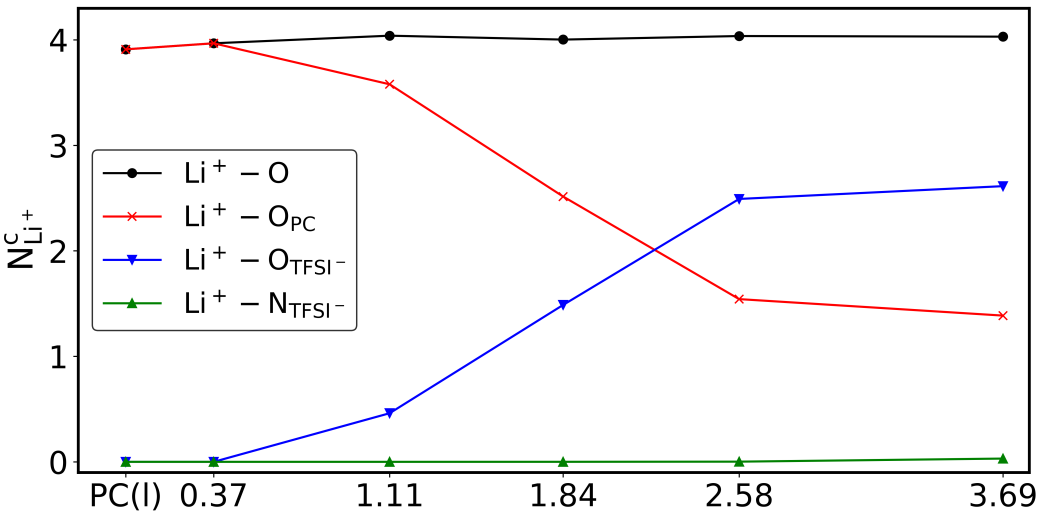

Fig. S9 Coordination numbers of Li^+ to O atoms and N atoms in electrolytes at different LiTFSI concentrations. Black line corresponds to all O atoms surrounding Li^+, red and blue line are for O atoms in PC and $TFSI^-$, respectively, and green line is for N atoms in $TFSI^-$.

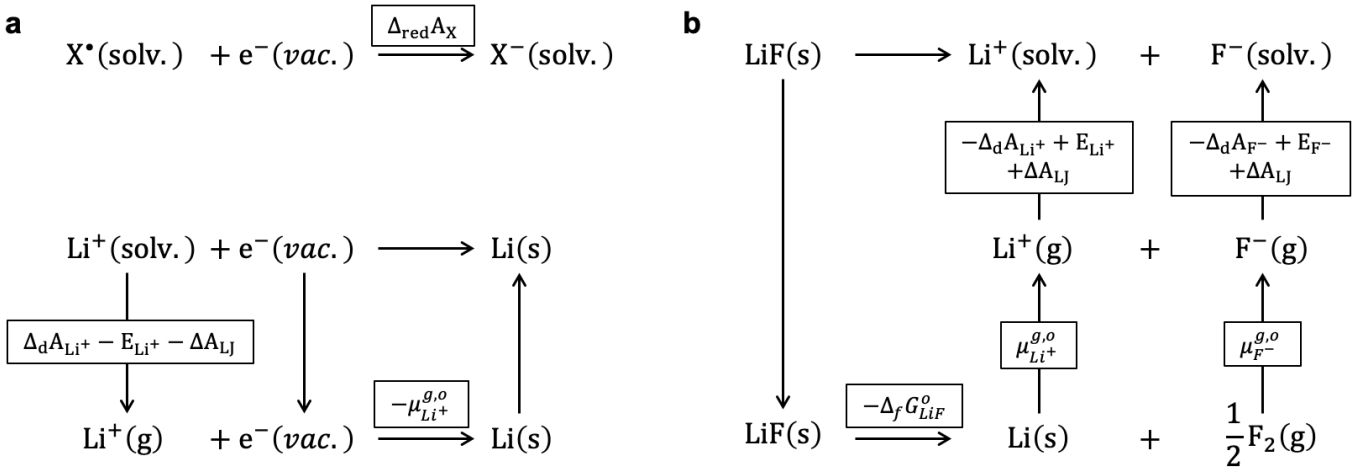

Fig. S10 Thermodynamic cycles for (a) redox potentials vs. $Li^+/Li(s)$ and (b) dissolution free energy of LiF.

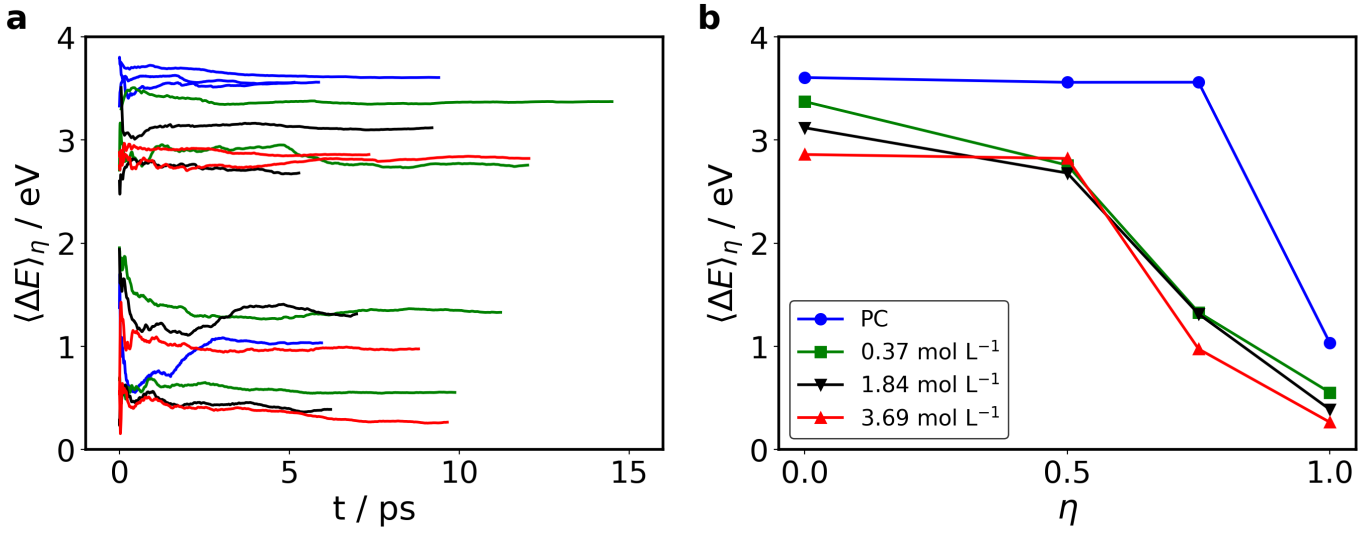

Fig. S11 Time accumulating averages of vertical energy gaps $\langle \Delta_{\mathrm{red}} \mathrm{E} \rangle_\eta$ and thermodynamic integration for reduction free energy $\Delta_{\mathrm{red}} \mathrm{A}$ of TFSI^- as a function of coupling parameter η for electrolytes at different TFSI^- concentrations.

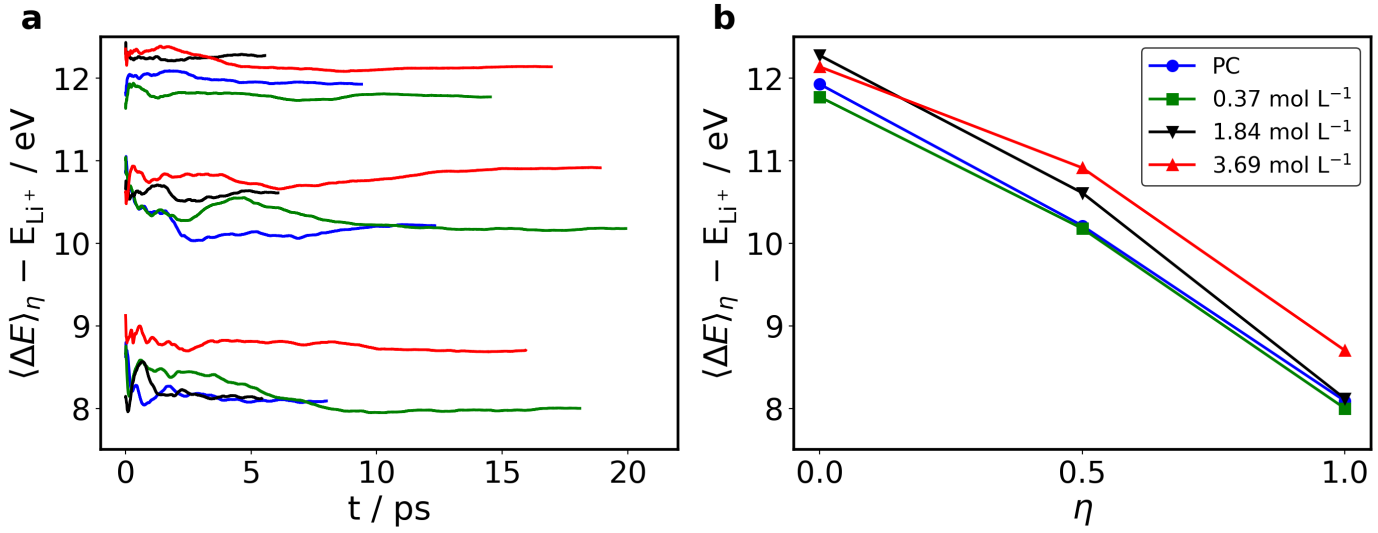

Fig. S12 Time accumulating averages of vertical energy gaps $\langle \Delta_d E \rangle_\eta$ and thermodynamic integration for desolvation free energy $\Delta_d A$ of Li^+ as a function of coupling parameter η for electrolytes at different $TFSI^-$ concentrations.

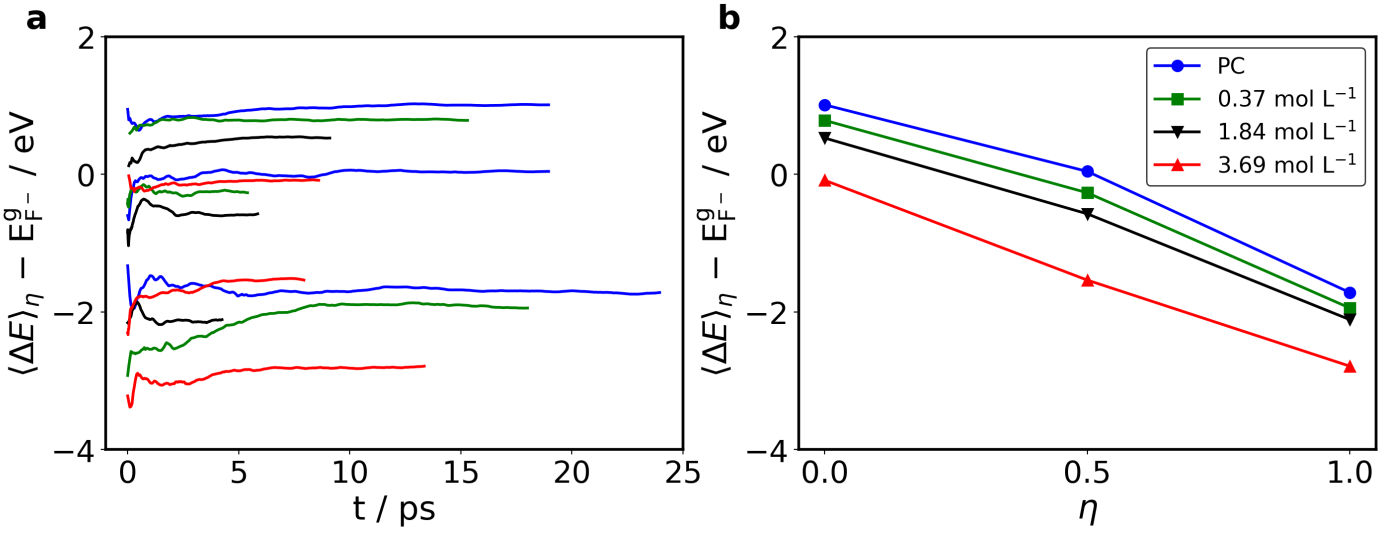

Fig. S13 Time accumulating averages of vertical energy gaps $\langle \Delta_d E \rangle_\eta$ and thermodynamic integration for desolvation free energy $\Delta_d A$ of F^- as a function of coupling parameter η for electrolytes at different $TFSI^-$ concentrations.

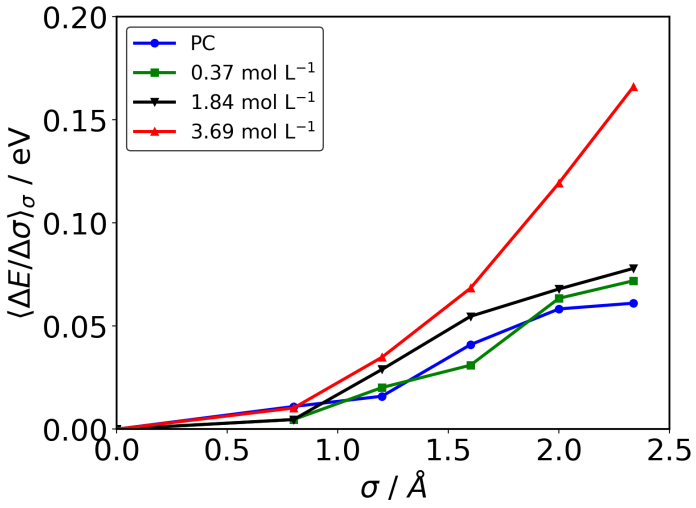

Fig. S14 Averaged derivative of the potential energy $\langle \Delta E/\Delta\sigma \rangle_\sigma$ as a function of σ in the Lennard-Jones potential. Integration from $\sigma = 0$ to 2.337Å of the curves yields the cavity formation energies ΔA_{LJ}.

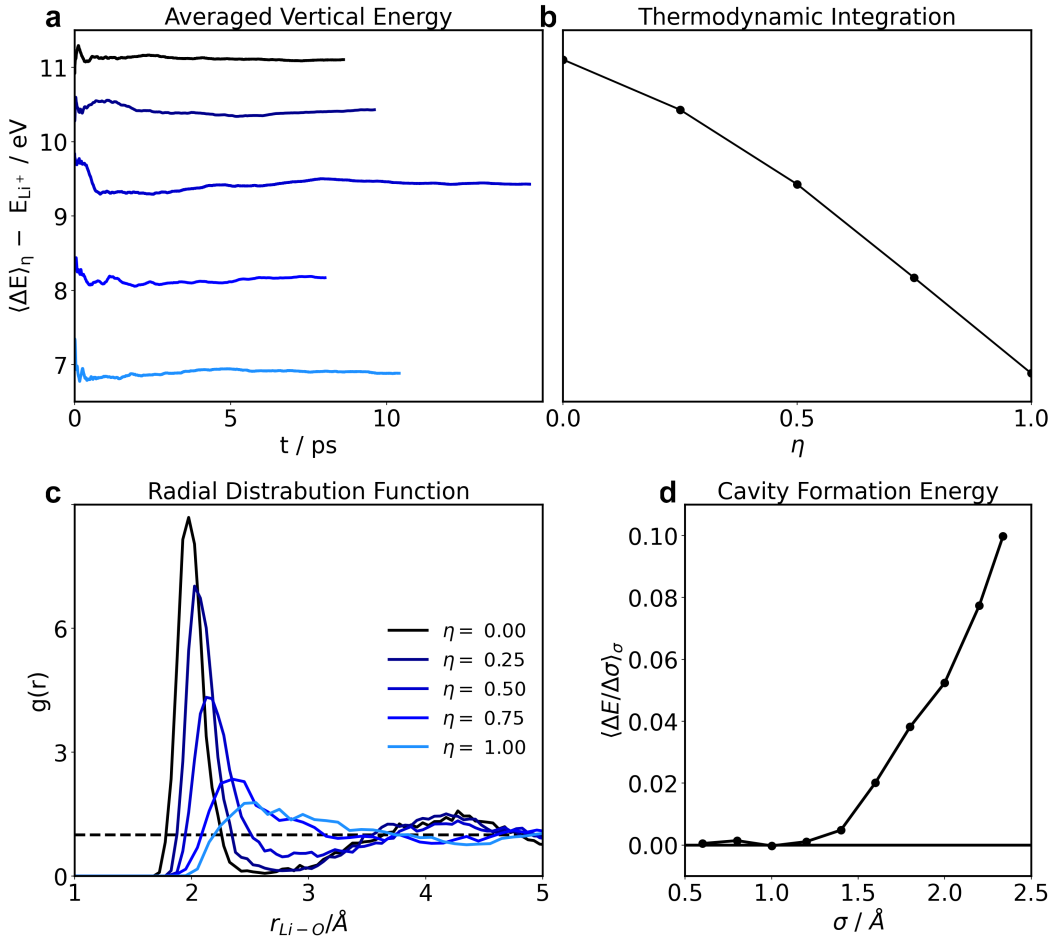

Fig. S15 (a) Time accumulating averages of vertical energy gaps $\langle \Delta_d E_{Li^+} \rangle_\eta$ and (b) thermodynamic integration for $\Delta_d A_{Li^+}$ in bulk water as a function of coupling parameter η. (c) Radial distribution functions of Li^+ and O in water for different η are plotted for comparison. (d) Averaged derivative of the potential energy $\langle \Delta E/\Delta\sigma \rangle_\sigma$ as a function of σ in the Lennard-Jones potential in bulk water.

Notes and references

1 J. Cheng, M. Sulpizi and M. Sprik, *J. Chem. Phys.*, 2009, **131**, 154504.

2 X.-H. Yang, A. Cuesta and J. Cheng, *J. Phys. Chem. B*, 2019, **123**, 10224–10232.

3 C. Adriaanse, J. Cheng, V. Chau, M. Sulpizi, J. VandeVondele and M. Sprik, *J. Phys. Chem. Lett.*, 2012, **3**, 3411–3415.

4 J. Cheng, X. Liu, J. VandeVondele, M. Sulpizi and M. Sprik, *Accounts Chem. Res.*, 2014, **47**, 3522–3529.

5 J. G. Kirkwood, *J. Chem. Phys.*, 1935, **3**, 300–313.

6 J. Cheng and M. Sprik, *Phys. Chem. Chem. Phys.*, 2012, **14**, 11245–11267.

7 M. Sulpizi and M. Sprik, *Phys. Chem. Chem. Phys.*, 2008, **10**, 5238–5249.

8 D. R. Lide *et al.*, *CRC handbook of chemistry and physics, internet version 2005*, 2005.

9 Z. Wang, W. Gao, X. Huang, Y. Mo and L. Chen, *J. Raman Spectrosc.*, 2001, **32**, 900–905.

10 J. VandeVondele, M. Krack, F. Mohamed, M. Parrinello, T. Chassaing and J. Hutter, *Comput. Phys. Commun.*, 2005, **167**, 103–128.

11 J. VandeVondele and J. Hutter, *J. Chem. Phys.*, 2007, **127**, 114105.

12 S. Goedecker, M. Teter and J. Hutter, *Phys. Rev. B*, 1996, **54**, 1703–1710.

13 C. Hartwigsen, S. Goedecker and J. Hutter, *Phys. Rev. B*, 1998, **58**, 3641–3662.

14 A. D. Becke, *Phys. Rev. A*, 1988, **38**, 3098–3100.

15 C. Lee, W. Yang and R. G. Parr, *Phys. Rev. B*, 1988, **37**, 785–789.

16 S. Grimme, J. Antony, S. Ehrlich and H. Krieg, *J. Chem. Phys.*, 2010, **132**, 154104.

17 K. Leung, *Phys. Chem. Chem. Phys.*, 2015, **17**, 1637–1643.

18 T. D. Kühne, *WIRES Comput. Mol. Sci.*, 2014, **4**, 391–406.

19 T. Musso, S. Caravati, J. Hutter and M. Iannuzzi, *Eur. Phys. J. B*, 2018, **91**, 1–8.

20 L. D. Gibson, J. Pfaendtner and C. J. Mundy, *J. Chem. Phys.*, 2021, **155**, 204703.

21 Y. Kameda, Y. Umebayashi, M. Takeuchi, M. A. Wahab, S. Fukuda, S.-i. Ishiguro, M. Sasaki, Y. Amo and T. Usuki, *J. Phys. Chem. B*, 2007, **111**, 6104–6109.

22 J. W. Smith, R. K. Lam, A. T. Sheardy, O. Shih, A. M. Rizzuto, O. Borodin, S. J. Harris, D. Prendergast and R. J. Saykally, *Phys. Chem. Chem. Phys.*, 2014, **16**, 23568–23575.

23 S. Rajamani, T. Ghosh and S. Garde, *J. Chem. Phys.*, 2004, **120**, 4457–4466.

24 S. Li, Z. Cao, Y. Peng, L. Liu, Y. Wang, S. Wang, J.-Q. Wang, T. Yan, X.-P. Gao, D.-Y. Song *et al.*, *J. Phys. Chem. B*, 2008, **112**, 6398–6410.

25 M. Takeuchi, Y. Kameda, Y. Umebayashi, S. Ogawa, T. Sonoda, S.-i. Ishiguro, M. Fujita and M. Sano, *J. Mol. Liq.*, 2009, **148**, 99–108.

26 K. Leung, S. B. Rempe and O. A. von Lilienfeld, *J. Chem. Phys.*, 2009, **130**, 204507.

27 K. Leung, *Chem. Phys. Lett.*, 2013, **568**, 1–8.

28 M. Frisch, G. Trucks, H. Schlegel, G. Scuseria, M. Robb, J. Cheeseman, G. Scalmani, V. Barone, G. Petersson, H. Nakatsuji *et al.*, *Gaussian 16*, 2016.